Tellurium Quantum Dots/Graphene Oxide-Based RRAM with improved Resistive Switching for high-precision image recognition applications

Jing-Yao Bian(卞景垚) [1†], Jingjing Shao(邵京京) [1], Li Li(李莉) [1], Yongxing Zhu(朱永兴) [2], Zhong-Qiang Wang(王中强) [2†], Ye Tao(陶冶) [2], Hong-Wei Ding(丁红伟) [1], and Feng Wang(王丰) [1†]

[1] Heilongjiang University of Science and Technology, School of Science, Harbin 150020, China

[2] State Key Laboratory of Integrated Optoelectronics, Key Laboratory for UV Light-Emitting Materials and Technology (Northeast Normal University), Ministry of Education, 5268 Renmin Street, Changchun 130024, China

With the rapid expansion of the big-data era, resistive random access memory (RRAM) has attracted considerable interest for high-density data storage and neuromorphic computing applications. However, its practical deployment remains limited by significant variability in resistive switching (RS) parameters, mainly caused by the stochastic formation and rupture of conductive filaments. In this work, we reported a RRAM based on a tellurium quantum dots (Te QDs)/graphene oxide (GO) film, which effectively improves the uniformity of RS characteristics. Benefiting from the incorporation of Te QDs, the device exhibits significantly reduced parameter fluctuations, including a narrowed switching voltage distribution, highly uniform SET and RESET voltages, and fast switching speed. Based on the electrical characteristics, the embedded Te QDs are proposed to provide localized transport sites that may promote the formation of preferential carrier conduction pathways within the GO matrix. Spike-time-dependent plasticity and multiple synaptic functions are further successfully emulated. In addition, leveraging a 100 × 100 memristive array, image pattern recognition is successfully demonstrated. These results highlight a viable route toward highly reliable memristive devices and advanced artificial neural networks for intelligent applications.

Keywords: Tellurium Quantum Dots; Memristor; Resistive Switching; Artificial neural networks

PACS: 73.40.Rw, 81.07.-b, 87.19.lv

1. Introduction

The global volume of digital information has grown rapidly in recent years, driven by advances in large-scale artificial intelligence models and data-intensive technologies.[1,2] This explosive data growth has intensified the demand for alternative

† Corresponding author. E-mail: bianjingyao@usth.edu.cn
† Corresponding author. E-mail: wangzq752@nenu.edu.cn
† Corresponding author. E-mail: wangfeng5678@163.com

data storage technologies, as silicon semiconducting devices are approaching fundamental physical and theoretical limits in further downscaling.[3-5] Moreover, the von Neumann bottleneck, which arises from the limited data transfer efficiency between physically separated memory and processing units, has driven the development of next-generation memory technologies with high density and fast operation.[6,7] Resistive random-access memory (RRAM) has emerged as a highly promising candidate for next-generation computing and data storage applications.[8-11] RRAM operates through electrically driven resistance modulation and exhibits several advantageous characteristics, such as high scalability, three-dimensional integration capability, low power consumption, and fast switching speed. These features make it well-suited for in-memory computing applications aimed at overcoming the von Neumann bottleneck.

Diverse material systems, including oxides, organic polymers, two-dimensional materials, and metal chalcogenide quantum dots,[12-18] have been demonstrated to exhibit resistive switching (RS) behavior. In particular, graphene oxide (GO) has widely studied due to its cost-effective solution processability, tunable film thickness, and excellent mechanical flexibility. Kim et al. demonstrate a GO-based memristive logic-in-memory circuit, enabling neuromorphic computing with ultralow power consumption.[19] Singh et al. observed and characterized RS induced memristive behavior in GO thin films, highlighting their potential for nonvolatile memory applications.[20] These studies have advanced GO-based memristors toward neuromorphic computing and practical applications. In parallel, tellurium quantum dots (Te QDs) exhibit pronounced quantum confinement effects, which critically influence their electronic properties, including charge trapping and localized field effects.[21-24] The Te QDs provide an ideal platform for fabricating memristors with tunable electrical properties. Incorporating Te QDs into GO is therefore expected to improve the stability and reliability of resistive switching. To the best of our knowledge, such investigations have not yet been reported.

Previous studies have demonstrated the potential of QDs-based materials for regulating the electrical and synaptic characteristics of memristive devices. For example, Yan et al. reported a graphene oxide quantum dot (GQD)-based memristor with progressive conductance tuning, in which the bidirectional conductance modulation was associated with the coexistence of tunneling and electrochemical metallization effects.[25] The device further enabled synaptic functions such as spike-timing-dependent plasticity and paired-pulse facilitation. Li et al. subsequently demonstrated carbon-dot-based memristors with improved resistance-state uniformity, lower power consumption, and faster response, and further explored their applications in artificial biosynaptic learning.[26] These studies demonstrate that quantum dots or carbon dots can be effectively incorporated into resistive switching devices to regulate electrical transport and improve neuromorphic performance.

In our work, Te QDs were synthesized via an ultrasonic exfoliation method to fabricate the Al/Te QDs-GO/ITO memristive device. The resulting devices exhibit robust bipolar nonvolatile resistive switching with a narrowed switching voltage distribution and enhanced cycling stability. Furthermore, increasing the doping

concentration of QDs enables a transition to analog resistive switching, allowing the emulation of synaptic functions. Image pattern recognition is achieved using artificial neuromorphic networks, with a recognition accuracy of 95.4%. This study provides a feasible approach to realizing both highly reliable resistive switching and neuromorphic computing.

2. Experiment

Synthesis of Te QDs: 0.5 g of tellurium (Te) powder (Macklin, CAS number: 13494-80-9) was finely ground in an agate mortar and subsequently transferred to a beaker. 50 mL of N-methyl-2-pyrrolidone (NMP, Macklin, CAS number: 2687-44-7) was added, and the mixture was sonicated in an ultrasonic bath at room temperature for 4 h. The resulting dark-brown suspension was centrifuged at 2000 rpm for 15 min, and the clear brown supernatant was collected as the Te QDs solution.

Device Fabrication: First, an ITO substrate was ultrasonically cleaned in trichloro ethylene, acetone, ethanol, and distilled water for 10 min each to remove impurities at room temperature, then dried using N_2 gas. Secondly, the Te QDs powder was dispersed by ultrasonication at a power of 40 W for 10 min at 25 °C. The Te QDs powder was dispersed in a graphene oxide (GO) solution to prepare Te QDs/GO suspensions with Te QDs mass fractions of 0%, 5%, 10%, and 20%, respectively, where the mass fraction was defined as $M_{Te\ QDs}/(M_{Te\ QDs}+M_{GO})\times 100\%$. The mixtures were continuously stirred at 400 rpm for 4 h to ensure uniform dispersion. Then the Te QDs-GO solution in two drops was spin-coated on the ITO substrate at 500 rpm for 5 s and 2000 rpm for 10 s. Finally, an Al top electrode was deposited by thermal evaporation using a shadow mask.

Characterization and Electrical Measurements: The thickness of the Te QDs–GO film was characterized by atomic force microscopy (AFM; Dimension Icon, Bruker). The current–voltage (I–V) characteristics were measured using an integrated test platform (Metatest corporation, Scanpro 100) equipped with several source meters (Keithley, 2600 series) under dark ambient conditions at room temperature. Electrical pulses were generated using arbitrary waveform generators (3390, Keithley; TGA12104, TTI), and the corresponding signals were monitored using an oscilloscope (DSOS404A, Keysight). Unless otherwise specified, all electrical measurements in this work were conducted at room temperature (24 °C) and a relative humidity of 30%.

3. Results and discussion

Figures 1(a) and 1(b) schematically depict the proposed memristor featuring a vertical Al/Te QDs-GO/ITO architecture, analogous to a biological synapse. The detailed fabrication procedures of the memristor are described in the Experimental Section. A cross-sectional scanning electron microscope image (Figure 1(c)) reveals a uniform resistive switching layer with a thickness of approximately 40 nm. As shown in Figures 1(d) and 1(g), the transmission

electron microscopy (TEM) images indicate that the Te QDs embedded in the GO layer exhibit a narrow size distribution with an average diameter of ≈ 6.45 nm. Such a well-controlled QD size is beneficial for suppressing fluctuations in stochastic conductive filament formation, as discussed in detail in the Mechanism section. The high-resolution TEM (HRTEM) image and selected area electron diffraction (SAED) patterns indicate the good crystallinity of Te

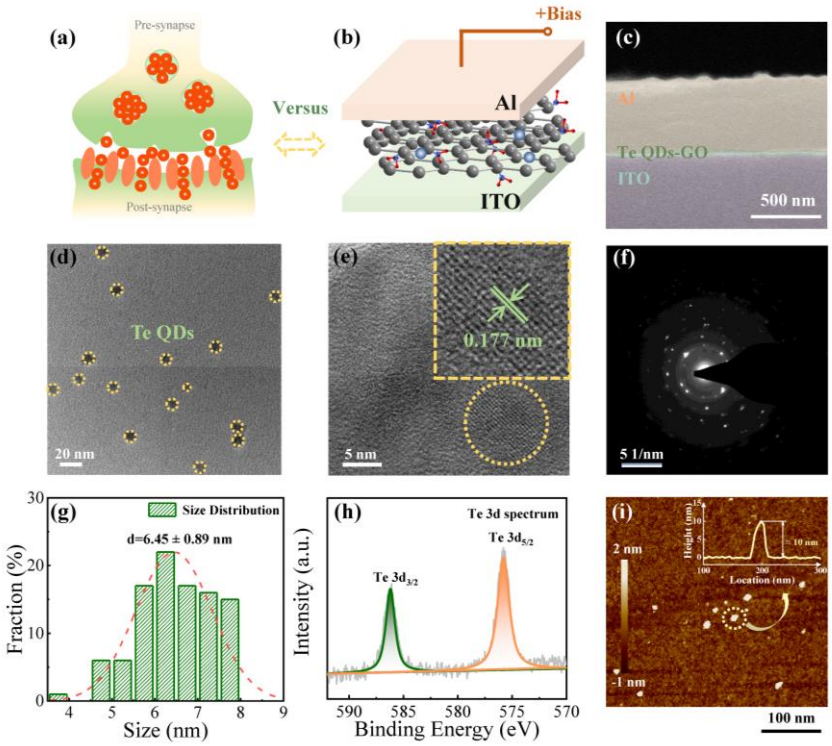


Figure 1. Vertical memristor based on Te QDs–GO. (a-c) Device structure and cross-sectional SEM image of the Te QDs-GO nanocomposite-based memristor. (d) TEM image of the dispersive Te QDs. (e) and (f) HRTEM image and SAED patterns of the Te QDs. (g) Statistical size distribution of the Te QDs. (h) The 3d core-level X-ray photoelectron spectroscopy results of the Te QDs. (i) AFM image and corresponding height profile of the Te QDs.

QDs (Figures 1(e) and 1(f)). Clear lattice fringes with an interplanar spacing of 0.177 nm are observed from the line profile (yellow line) in the marked region, corresponding to the (102) crystallographic plane of tellurium, as consistent with the literature.[23] The X-ray photoelectron spectroscopy (XPS) spectrum of the Te QDs is presented in Figure 1(h). The prominent peaks located at 283.4, 575.8, and 586.2 eV are assigned to C 1s, Te $3d_{5/2}$, and Te $3d_{3/2}$, respectively.[27-29] The splitting of the Te 3d core level originates from spin-orbit coupling. Atomic force microscopy (AFM) measurements were further performed to evaluate the size of the Te QDs, as shown in Figure 1(i). The height profile of representative Te QDs is approximately 10 nm. The above results indicate that Te QDs exhibit good crystallinity and controllable size,

providing a solid foundation for subsequent electrical characterization.

The incorporation of Te QDs effectively guides the growth direction and spatial distribution of conductive filaments, thereby significantly improving the RS performance of the device. To further evaluate this performance, the reproducibility of RS characteristics for GO-based devices, both without and with 5% Te QDs, was systematically investigated. As shown in Figures 2(a) and 2(b), the current-voltage (I-V) characteristic curves were measured under a compliance current of 500 μA. It can be clearly observed that the Te QDs-GO device exhibits more uniform and reproducible I-V switching behaviors, accompanied by an obvious reduction in cycle-to-cycle variability and switching voltage fluctuations. The retention characteristic of the Te QDs-GO

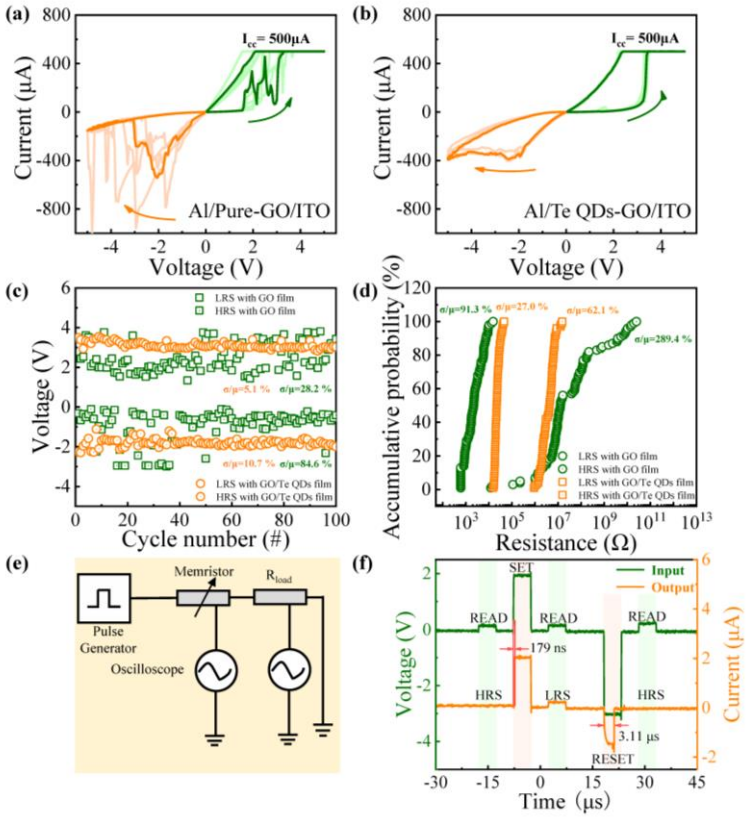


Figure S1. Electrical characteristics of Te QDs–GO-based vertical memristors. Current–voltage (I-V) characteristics of (a) the Al/Pure-GO/ITO and (b) the Al/Te QDs-GO/ITO device. The corresponding V_{SET}/V_{RESET} and HRS/LRS distributions of the device are shown in (c) and (d), respectively. (e) Schematic illustration of the pulse measurement setup, consisting of a pulse generator, an oscilloscope, the Al/Te QDs-GO/ITO memristor device, and a load resistor (1 MΩ). (f) Resistive switching speed of the Al/Te QDs-GO/ITO device measured under pulse operation.

device was shown in Figure S1. As compared in Figure 2(c), the relative distributions of the set voltage (V_{SET}) and reset voltage (V_{RESET}) become significantly narrower after the introduction of 5% Te QDs. The relative fluctuation, defined as the ratio of the standard deviation (σ) to the mean value (μ),[30] is markedly reduced with the incorporation of Te QDs, indicating

improved switching uniformity and enhanced operational stability. Furthermore, the statistical distributions of the high-resistance state (HRS) and low-resistance state (LRS) were analyzed for both devices, as shown in Figure 2(d). The Te QDs-GO device shows a tighter resistance distribution. For example, after incorporating Te QDs, the fluctuation in the LRS is reduced from 91.3% to 27%. This improvement can be attributed to the modification of the local electronic and interfacial environment by Te QDs, which may facilitate more localized and reproducible formation of conductive pathways and thereby reduce the stochasticity of the switching behavior. The statistical analysis of the device-to-device and array levels was provided in Figure S2. Furthermore, increasing the concentration of Te QDs to 10% and 20% induces analog RS behavior, making the device highly suitable for biomimetic applications such as artificial synapses (see Figures S3 and S4).

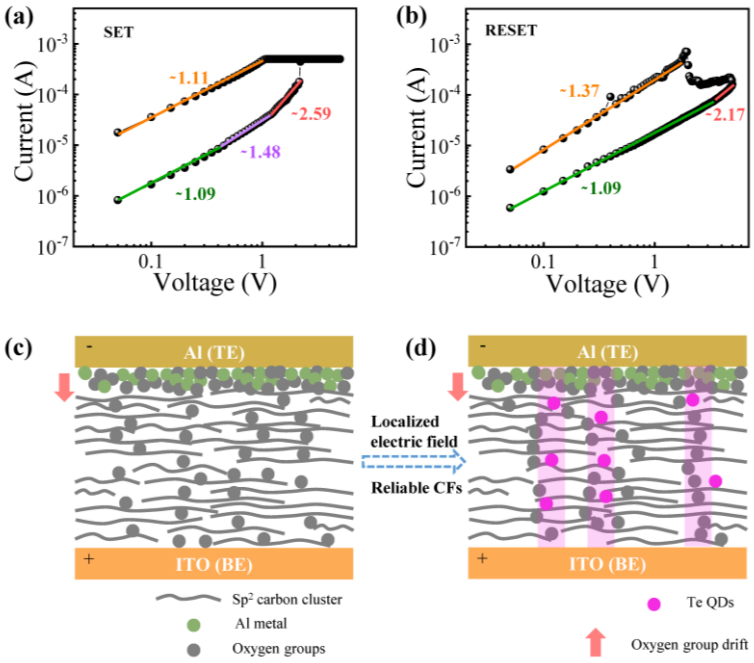


Figure 3. Electrical characteristics of Te QDs–GO-based vertical memristors. Double-logarithmic I-V characteristics and corresponding fitted conduction mechanisms under (a) positive and (b) negative voltage sweeps. (c) and (d) Schematic illustrations of the RS mechanism.

In addition, the RS speed characteristics of the device were investigated under a pulse-programming mode, and the representative RS responses are shown in Figures 2(e) and 2(f). The input signal generated by a waveform generator was designed as a voltage pulse sequence in the following order: $READ_{1st}$→SET→$READ_{2nd}$→RESET →$READ_{3th}$ pulse. Two READ pulses were applied before and after the SET (RESET) pulse to confirm the occurrence of the resistive switching transition. The pulse amplitudes and widths were set as follows: 2 V/5 μs for the SET pulse, -3 V/5 μs for the RESET pulse, and 0.1 V/5 μs for both READ pulses. The voltage drop across the load resistor was defined as the output signal. The SET switching time was defined as the time delay between the input and output signals, while the RESET time was

determined from the duration of the output pulse, as illustrated in Figures 2(e) and 2(f). The extracted response times were approximately 179 ns for the SET process and 3.11 μs for the RESET process in the Te QDs-GO device, demonstrating fast switching dynamics and highlighting its potential for low-power operation. These results confirm that the 5% Te QDs-GO device possesses reliable high-speed switching capability and stable RS characteristics.

To elucidate the beneficial role of Te QDs in the Al/Te QDs-GO/ITO memristor, the underlying RS mechanism was systematically investigated. The conduction mechanisms during the SET and RESET processes were analyzed by replotting the I-V characteristics on a double-logarithmic scale (Figures 3(a) and 3(b)). In LRSs, the fitted slopes in both positive and negative voltage regions are close to 1, indicating typical Ohmic conduction behavior, which is consistent with the formation of a stable conductive channel. In contrast, the HRS exhibits distinct nonlinear characteristics. Under positive voltage sweep, the slope evolves from 1.09 to 1.48 and further to 2.59 with increasing voltage. Similarly, in the negative voltage region, two linear regimes with slopes of approximately 1.09 and 2.17 are observed. These results agree well with the classical space-charge-limited conduction (SCLC) model.[31,32] As illustrated in Figures 3(c) and 3(d), pristine GO contains a high density of sp^3-hybridized carbon domains associated with abundant oxygen-containing functional groups. Upon application of an external electric field, these oxygen functionalities dissociate from the carbon framework and drift toward the Al electrode, resulting in the formation of numerous oxygen vacancies within the switching layer. This process triggers a structural transition from sp^3- to sp^2-hybridized carbon, leading to the formation of conductive pathways composed of interconnected sp^2 domains,[33,34] thereby switching the device from the initial HRS to the LRS. The incorporation of Te QDs modifies the local electronic and interfacial environment within the switching layer, which may contribute to a more confined and reproducible evolution of conductive pathways. This effect, together with the intrinsic charge trapping/de-trapping and ion migration processes in the Te QDs/GO composite, contributes to the improved uniformity and reduced stochasticity of the resistive switching behavior. Conversely, under a reverse (negative) bias, the conductive filament becomes partially disrupted near the Al electrode, leading to the formation of a gap region. This rupture of the filament drives the device to switch from the LRS back to the HRS.

Interest-driven learning reflects an intrinsic motivation that supports autonomous learning, engagement, and memory retention.[35,36] As illustrated in Figure 4(a), both interest and repetitive learning play crucial roles in memory formation and consolidation. The fabricated device was engineered to emulate this learning mechanism. For adolescents, elevated levels of learning interest promote longer retention of acquired knowledge and cultivate a positive learning attitude, thereby enhancing both motivation and memory performance. To stimulate interest-based learning, the device was initially set to a low-conductance state by applying a 2 V voltage. Subsequently, “interest voltages” of 200 mV, 500 mV, and 1 V were sequentially applied to read the current states of the device, as illustrated in Figures 4(b)-4(d). The results indicate that with increasing applied interest voltage, the device

maintains its current for a longer duration. This evidence demonstrates that the device effectively emulates the principle whereby greater interest in a subject leads to stronger and more persistent memory retention.

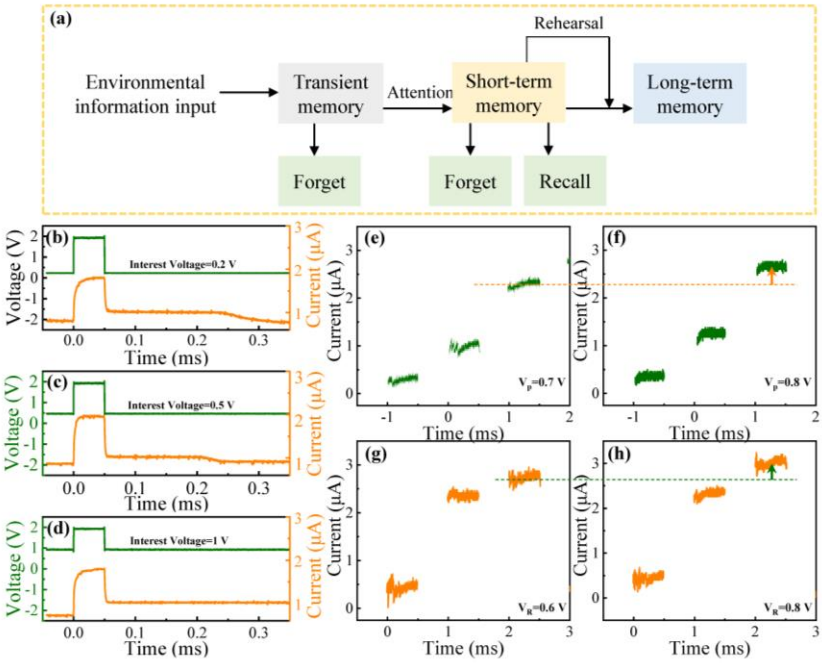


Figure 4. Interest-driven learning enabled by Te QDs-GO vertical memristors. (a) The rule of learning and memory. (b-d) The degree of learning and memory under different interest voltages of 200 mV, 500 mV and 1 V, respectively. (e) and (f) Current evolution under different preview voltage (0.7 V and 0.8 V, respectively). (g) and (h) Current variation induced by different review voltages, 0.6 V and 0.8 V, respectively.

The preview and review processes, which are two critical components for memory retention,[37] are successfully emulated using the Te QDs-GO device. In this simulation, a higher conductance corresponds to a stronger memory effect. The learning process is divided into three stages: preview, formal learning, and review. To evaluate the influence of preview and review on memory retention, we first tested the memory effect of the device under formal learning only, without preview or review stages. During this process, a learning voltage (V_L) of 2 V, representing the formal learning stage, was applied to the device to probe its conductance state. Figure S5(a) shows the voltage waveform, including the preview voltage (V_P), learning voltage (2 V), and reading voltage (V_{read}, 0.1 V). The reading voltage was applied to read the current states at different points: before and after the preview stage, and after the formal learning stage. The influence of varying the preview (V_P) and review (V_R) voltages on the current response was further investigated. When V_P and V_R were raised from 0.7 V to 0.8 V while maintaining constant learning voltage (V_L), the device exhibited an increased final current, as shown by the yellow line in Figures 4(e)-4(f), indicating an enhanced level of learning. Next, we investigated the influence of the review process on memory retention. The pulse waveforms applied to the device are presented in Figure S5(b). As illustrated in Figures 4(g)-4(h), the memory

effect becomes increasingly pronounced as the review voltage (V_R) is raised, as highlighted by the green line. These observations indicate that a stronger review stimulus reinforces the device's current state, thereby enhancing memory retention. The experimental results clearly demonstrate that incorporating both preview and review stages in the learning process leads to a substantial improvement in memory performance, highlighting the potential of memristor devices for applications in computational neuroscience and machine learning.

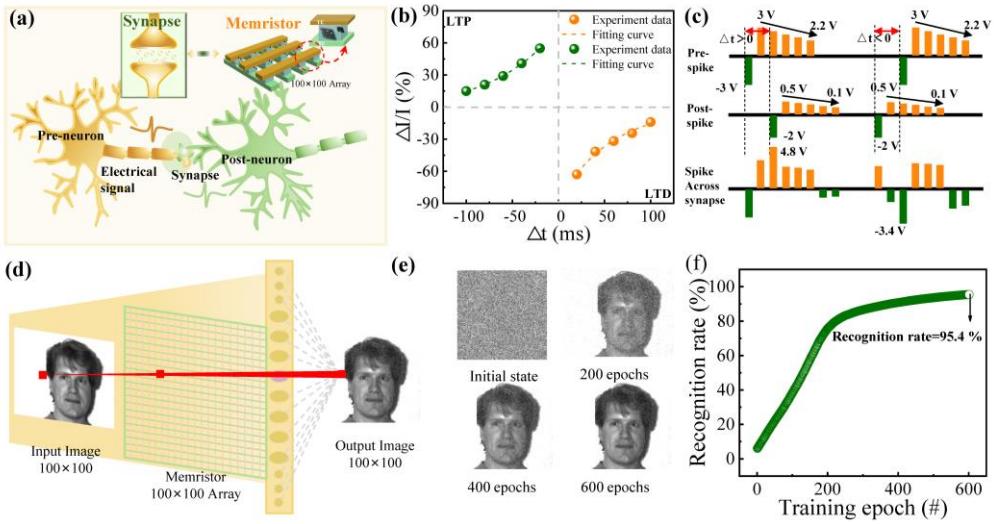


Figure 5. Image learning in Te QDs-GO vertical memristors. (a) Schematic illustration of a biological synapse (left) and the corresponding Al/Te QDs-GO/ITO memristor (right). (b) STDP-like curve fitted from experimental measurements. (c) Implementation of STDP via pulse amplitude modulation. (d) Schematic of the ANN architecture composed of memristors for image recognition. (e) Evolution of image patterns during learning, showing initial, intermediate, and final states. (f) Learning accuracy of the ANN as a function of the number of training epochs.

Memristive devices are regarded as an ideal hardware platform for implementing neuromorphic computing due to their intrinsic ability to emulate synaptic behaviors.[38-41] Figure 5(a) depicts the rationale behind developing memory devices that emulate biologically realistic synaptic functions, highlighting the importance of bridging artificial and neural information processing. The conduction mechanism in the Al/Te QDs-GO/ITO memory closely mimics the ion channels and Ca^{2+} dynamics of biological synapses. As a key form of synaptic plasticity, the spike-timing-dependent plasticity (STDP) learning rule enables modulation of synaptic weights through temporally correlated pre- and post-synaptic spikes.[42,43] The time difference between paired spikes (i.e., $\Delta t = t_{post} - t_{pre}$) determines whether long-term potentiation (LTP) occurs at $\Delta t < 0$ (i.e., the presynaptic spike precedes the postsynaptic spike) or long-term depression (LTD) occurs at $\Delta t > 0$. This spike-timing-dependent modification is considered a fundamental learning feature required for executing complex recognition functions in biological systems. To harness the capability of pulse amplitude modulation for implementing STDP, the spike waveform was designed as illustrated in Figure 5(c). STDP was implemented using a pulse amplitude modulation scheme. The pulse amplitudes for the presynaptic

spikes were set sequentially to -3, 3, 2.8, 2.6, 2.4, and 2.2 V with a time interval of 20 ms, while the postsynaptic spike amplitudes were -2, 0.5, 0.4, 0.3, 0.2, and 0.1 V with the same time interval. Using this signaling protocol, the STDP-like behavior was successfully reproduced in the electronic synapse devices, as shown in Figure 5(b). The change in synaptic weight, Δw, as a function of the spike time difference, Δt, can be quantitatively described by an exponential fitting function:[44-46]

$$\triangle W = \begin{cases} A_{-}e^{\frac{\triangle t}{\tau -}}, & t<0 \\ A_{+}e^{\frac{\triangle t}{\tau +}}, & t>0 \end{cases}$$

Here, A_+ and A_- represent the amplitude parameters for LTP and LTD, respectively, while $\tau+$ and $\tau-$ denote the corresponding time constants. The change in synaptic weight, ΔW, was defined as $\Delta W = (G_2\text{-}G_1)/G_1 \times 100\%$, where G_2 and G_1 are the conductance after and before voltage application, respectively. The fitted STDP model enables accurate simulation of neural network dynamics for image recognition. To extend this model to the processing of spatiotemporal patterns, an artificial neuromorphic network (ANN) was implemented using a memristive array, as depicted in Figure 5(d). In this architecture, each memristor functions as a synapse connecting pre- and post-neurons, with the synaptic weight represented by the gray level of each pixel. The initial input image was divided into 100 × 100 pixels, and the gray-scale variations of each pixel were stored in real time in the corresponding memristor cells during successive learning epochs. It should be noted that the 100 × 100 array in this work represents a virtual synaptic array implemented in software. The experimentally measured LTP/LTD characteristics were fitted and mapped onto the array for the software-based neuromorphic image-learning simulation, rather than being directly implemented using a physically fabricated 100 × 100 hardware array. Figure 5(e) presents the evolution of the image patterns during the learning process across different numbers of epochs. It is evident that the ANN achieves high-accuracy image recognition after 600 epochs. For a quantitative assessment of learning efficiency, the recognition accuracy was evaluated every 10 epochs. As shown in Figure 5(f), the ANN achieved a final learning accuracy of 95.4%, demonstrating that the RRAM-based system can perform high-precision pattern recognition effectively.

4. Conclusion and perspectives

In summary, we have demonstrated a Te QDs-GO based RRAM with significantly improved resistive switching uniformity and reliability. The incorporation of Te QDs not only suppresses the stochastic variability of conductive filaments but also enables stable switching, owing to the preferential pathways provided by the ordered quantum dot arrangement. The device further exhibits versatile synaptic functionalities, including spike-timing-dependent plasticity, which are successfully emulated. A three-layer ANN constructed using the Te QDs-GO memristive device achieved a high image recognition accuracy of 95.4%, demonstrating its potential for practical neuromorphic computing applications. This work presents a practical strategy for improving both the performance and reliability of memristive devices, thereby laying the foundation for the development of robust

artificial neural networks in intelligent computing systems.

Acknowledgment

This work was supported by the Open Fund of the State Key Laboratory of Integrated Optoelectronics, the National Natural Science Foundation of China (52472149), the Fundamental Research Funds for Provincial Undergraduate Universities in Heilongjiang Province (No. 2022-KYYWF-0563), and the funding from Jilin Province (Grant Nos. 20240210001GX).

References

[1] Lv Z, Wang Y, Chen J, Wang J, Zhou Y and Han S-T 2020 *Chem. Rev.* **120** 3941-4006
[2] Lanza M, Sebastian A, Lu W D, Le Gallo M, Chang M-F, Akinwande D, Puglisi F M, Alshareef H N, Liu M and Roldan J B 2022 *Science* **376** eabj9979
[3] Wang J, Lv Z, Xing X, Li X, Wang Y, Chen M, Pang G, Qian F, Zhou Y and Han S-T 2020 *Adv. Funct. Mater.* **30** 1909114
[4] Bao H, Zhou H, Li J, Pei H, Tian J, Yang L, Ren S, Tong S, Li Y, He Y, Chen J, Cai Y, Wu H, Liu Q, Wan Q and Miao X 2022 *Front. Optoelectron.* **15** 23
[5] Zidan M A, Strachan J P and Lu W D 2018 *Nat. Electron.* **1** 22-29
[6] Chen X, Ke C, Sun B, Liang H, Qian Z, Wen Q, Tian D, Yang C, Xu M and Zhao Y 2025 *ACS Appl. Nano Mater.* **8** 12459-12489
[7] Xia Z, Sun X, Wang Z, Meng J, Jin B and Wang T 2025 *Nano-Micro Lett.* **17** 217
[8] Xing S, Wang Z, Wang Z, Li P, Fan X, Zhang Z, Zhang G, Kan J, Luo Q, Zhong S and Zhang Y 2025 *IEEE J. Electron Devices Soc.* **13** 383-389
[9] Ielmini D and Pedretti G 2025 *Chem. Rev.* **125** 5584-5625
[10] Ju S, Jang H, Park W, Jung S and Kim S 2025 *Appl. Surf. Sci.* **697** 162973
[11] Shen Z, Zhao C, Qi Y, Xu W, Liu Y, Mitrovic I Z, Yang L and Zhao C 2020 *Nanomaterials* **10** 1437
[12] Fu L, Pan G, Hao R, Fan X and Li Y 2025 *Chinese Phys.* B **34** 077201
[13] Yu Z-Q, Jia J-H, Ou M-L, Sun T-Y and Xu Z-M 2025 *Chinese Phys. B* 34 127302
[14] Imran A, He X, Tabassum H, Zhu Q, Dastgeer G, Liu J, Sulaman M, Ali M, Xue F, Hanagata N and Xu M 2024 *Mater. Today Nano* **26** 100473
[15] Wang Y, Zha Y, Bao C, Hu F, Di Y, Liu C, Xing F, Xu X, Wen X, Gan Z and Jia B 2024 *Adv. Mater.* **36** 2311524
[16] Chen J, Zhou Z, Kim B J, Zhou Y, Wang Z, Wan T, Yan J, Kang J, Ahn J-H and Chai Y 2023 *Nat. Nanotechnol.* **18** 882-888
[17] Huang X, Wang Y, Huang H, Duan L and Guo T 2024 *Chinese Phys. B* 33 017303
[18] Teja Nibhanupudi S S, Roy A, Veksler D, Coupin M, Matthews K C, Disiena M, Ansh, Singh J V, Gearba-Dolocan I R, Warner J, Kulkarni J P, Bersuker G and Banerjee S K 2024 *Nat. Commun.* **15** 2334
[19] Kim Y, Jeon S-B and Jang B C 2023 *Nanomaterials* **13** 710
[20] Singh A, Paliwal S, Upadhyaya A, Kumar Gupta S and Negi C M S 2024

Materials Today: Proceedings
[21] Nguyen D A, Park D Y, Jeong B G, Tran T U, Im H and Jeong M S 2022 *Appl. Surf. Sci.* **581** 152398
[22] Yan X, Pei Y, Chen H, Zhao J, Zhou Z, Wang H, Zhang L, Wang J, Li X, Qin C, Wang G, Xiao Z, Zhao Q, Wang K, Li H, Ren D, Liu Q, Zhou H, Chen J and Zhou P 2019 *Adv. Mater.* **31** 1805284
[23] Wang S, Gong X, Wei J, Du L, Wang F, Lai S, Shao X, Gao W and Wang C 2025 *Front. Phys.* **20** 034401
[24] Chen X, Feng H, Xian H, Zheng X, Lin X, Zhou W, Hu Y, Chen Y, Huang C and Ye X 2025 *Int. J. Biol. Macromol.* **312** 144101
[25] Yan X, Zhang L, Chen H, Li X, Wang J, Liu Q, Lu C, Chen J, Wu H and Zhou P 2018 *Adv. Funct. Mater.* **28** 1803728
[26] Li X, Pei Y, Zhao Y, Song H, Zhao J, Yan L, He H, Lu S and Yan X 2022 *Mater. Chem. Front.* 2022, **6** 1098–1106
[27] Guo J, Huang J, Gu S, Lin L, Zhang Y, Wang X, Liu Y, Gong T, Lin Y, Yu B, Huang W and Zhang X 2025 *IEEE Electron Device Lett.* **46** 68-71
[28] Bian J, Li Z, Liang S, Tao Y, Wang Z, Zhu Y, Wang C, Xu H and Liu Y 2025 *Adv. Sci.* **12** e13647
[29] Bian J, Zhu Y, Tao Y, Wang Z, Zhao X, Lin Y, Xu H and Liu Y 2025 *Sci. China Mater.* **68** 2488-2496
[30] Tian Q, Zhao X, Zhang X, Lin H, Wang D, Xing G, Wang Z, Lin Y, Xu H and Liu Y 2021 *Appl. Phys. Lett.* **119** 143505
[31] Ge S, Guan X, Wang Y, Lin C-H, Cui Y, Huang Y, Zhang X, Zhang R, Yang X and Wu T 2020 *Adv. Funct. Mater.* **30** 2002110
[32] Ding G, Han S-T, Kuo C-C, Roy V A L and Zhou Y 2023 *Small Struct.* **4** 2200150
[33] Xiong W, Zhang G, Bao D-L, Lu J, Gao L, Li Y, Zhang H, Ruan Z, Hao Z, Gao H-J, Chen L and Cai J 2025 *Nat. Commun.* **16** 690
[34] Wu J, Yang X, Chen J, Li S, Zhou T, Cai Z, Lian X and Wang L 2024 *Nanotechnol. Rev.* **13** 20230181
[35] Anwar S, Choirudin C, Fitria Ningsih E, Dewi T and Maseleno A 2019 *Al-Jabar : Jurnal Pendidikan Matematika* **10** 135-150
[36] Tan A L, Gillies R and Jamaludin A 2021 *Educ. Sci.* **11** 379
[37] Hernández C, Cárdenas C, Romero P and Hernández M 2017 *Inf. Tecnol.* **28** 119-128
[38] Wang K, Hu Q, Gao B, Lin Q, Zhuge F-W, Zhang D-Y, Wang L, He Y-H, Scheicher R H, Tong H and Miao X-S 2021 *Mater. Horiz.* **8** 619-629
[39] Shan X, Zhao C, Wang X, Wang Z, Fu S, Lin Y, Zeng T, Zhao X, Xu H, Zhang X and Liu Y 2022 *Adv. Sci.* **9** 2104632
[40] Wang Y, Zhu Y, Li Y, Zhang Y, Yang D and Pi X 2022 *Adv. Funct. Mater.* **32** 2107973
[41] Walfort S, Vu X T, Ballmaier J, Holle N, Vollmar N and Salinga M 2026 *Nat. Mater.* **25** 643-650
[42] Ilyas N, Wang J, Li C, Li D, Fu H, Gu D, Jiang X, Liu F, Jiang Y and Li W 2022

Adv. Funct. Mater. **32** 2110976
[43] Wu G, Zhang Z, Ba K, Zhang X, Zeng J, Bai C, Liu Q and Wang J 2023 *IEEE Electron Device Lett.* **44** 857-860
[44] Hao Z, Wang H, Jiang S, Qian J, Xu X, Li Y, Pei M, Zhang B, Guo J, Zhao H, Chen J, Tong Y, Wang J, Wang X, Shi Y and Li Y 2022 *Adv. Sci.* **9** 2103494
[45] Wang Y, Yin L, Huang W, Li Y, Huang S, Zhu Y, Yang D and Pi X 2021 *Adv. Intell. Syst.* **3** 2000099
[46] Zeng T, Su R, Tao Y, Lin Y, Shan X, Cheng Y, Wang Z, Zhao X, Xu H and Liu Y 2022 *Adv. Electron. Mater.* **8** 2200246